Title	Operando X-Ray Imaging of the Charge-Discharge Behavior of Zinc-Air Batteries
Authors	Wooseok KANG, Shumpei KUBOTA, Manabu KODAMA, Atsunori IKEZAWA, Hajime ARAI, Shuichiro HIRAI
Citation	Electrochemistry, Volume 92, Issue 8, Page 087003
Pub. date	2024, 7
DOI	https://doi.org/10.5796/electrochemistry.24-00053
Creative Commons	Information is in the article.

Electrochemistry
The Electrochemical Society of Japan

Received: May 20, 2024
Accepted: July 8, 2024
Published online: July 12, 2024
Issued: August 7, 2024

https://doi.org/10.5796/electrochemistry.24-00053

Article
Electrochemistry, 92(8), 087003 (2024)

Operando X-Ray Imaging of the Charge-Discharge Behavior of Zinc-Air Batteries

Wooseok KANG,[a] Shumpei KUBOTA,[a] Manabu KODAMA,[a,*,§]
Atsunori IKEZAWA,[b,§] Hajime ARAI,[b,§§] and Shuichiro HIRAI[a]

[a] *Department of Mechanical Engineering, School of Engineering, Tokyo Institute of Technology,*
2-12-1 Ookayama, Meguro-ku, Tokyo 152-8550, Japan
[b] *Department of Chemical Science and Engineering, School of Materials and Chemical Technology, Tokyo Institute of Technology,*
4259 Nagatsutacho, Midori-ku, Yokohama, Kanagawa 226-8502, Japan

* *Corresponding author: tanaka.m.ay@m.titech.ac.jp*

ABSTRACT

Zinc-air batteries are anticipated to be next-generation energy storage devices because of their high capacities compared with conventional secondary batteries. However, the growth of zinc dendrites and electrolyte decomposition can compromise battery performance. To solve those problems, a thorough understanding of electrolyte and electrode behavior is paramount. Therefore, this study employs operando X-ray transmission imaging to observe electrolyte and electrode behavior during charging and discharging, aiming to elucidate their influence on battery performance. Operando X-ray transmission imaging successfully captures bubble generation and zinc deposition in the zinc-air battery. During discharge, bubbles form on the zinc electrode surface through a reduction reaction, while the battery current is suppressed by hindering ion transportation and electrode surface reactions. During charging, a change in the zinc deposition mode is observed from dense deposition to dendrite deposition. This deposition mode change is dependent on the charging current density and zinc ion concentration in the electrolyte. With an increase in the current density and a decrease in the zinc ion concentration, the deposition mode rapidly changes. Through experiments altering both the current density and initial zinc ion concentration in the electrolyte, we effectively determined the operating conditions that hinder zinc dendrite formation.

Keywords : Zinc-air Battery, Operando Observation, X-ray Imaging, Zinc Dendrite

1. Introduction

In response to the urgent challenges posed by climate change, there is a growing emphasis on utilizing renewable energy sources. This trend underscores the critical need to expand the capacities of energy storage systems, which are vital for managing the variable output from renewable energy sources. Among the various energy storage options, batteries utilizing electrochemical reactions are the most widely adopted because of their efficiency and capacity. Lithium-ion batteries, renowned for their high energy density, have rapidly evolved, becoming a primary power source for electric vehicles. However, the pursuit of batteries that can surpass lithium-ion batteries in terms of energy density and cost-effectiveness has led to the exploration of post-lithium-ion technologies, with zinc-air batteries emerging as a notable contender.[1]

Zinc-air batteries are anticipated to offer superior energy density compared with current lithium-ion batteries, boasting advantages such as the use of zinc, which is an abundant element, and the avoidance of flammable organic electrolytes.[2] These benefits make zinc-air batteries particularly appealing for large-scale energy storage and transportation applications, where high safety is required. Despite these advantages, zinc-air batteries are predominantly employed in small-scale, low-power applications, such as hearing aids.[3] Challenges including electrolyte depletion at the air electrode, hydrogen gas formation within the electrolyte, and dendrite growth on the zinc electrode during charge-discharge cycles significantly hinder their application as rechargeable secondary batteries, which are intended for prolonged use and undergoing numerous charge cycles.[4] Despite numerous studies aiming to understand these problems and enhance performance, many aspects of zinc-air batteries remain unexplored. For example, dendrites are known to form in regions characterized by low zinc ion concentrations and high charging current densities.[5] Additionally, zinc is susceptible to corrosive reactions in alkaline electrolytes, which can result in electrolyte decomposition and hydrogen evolution.[6] However, the precise mechanisms behind these phenomena have not been fully elucidated.[7]

To gain a better understanding of these phenomena, cell behavior needs to be analyzed using diverse data acquired under various operating conditions. Efforts to observe the interior of zinc-air batteries have employed various ex situ techniques, including electron microscopy, elemental analysis via X-ray diffraction (XRD), and X-ray computed tomography imaging.[8–10] In situ observations, such as two-dimensional transmission imaging by synchrotron X-ray techniques, are also gaining attention because of their advantages in combining data, including electrochemical records and ion concentration.[11] However, these in situ observations are mainly focused on real-time imaging, limiting the scope of the experiment to small areas. To promote the widespread use of zinc-air batteries, larger experimental regions should be analyzed by in situ techniques.

In this study, we focused on analyzing the phenomena that affect the charge-discharge performance of zinc-air batteries. By setting various experimental conditions based on zinc ion concentration and current density, this study aimed to determine the conditions that

---

[§] ECSJ Active Member
[§§] ECSJ Fellow

W. Kang orcid.org/0009-0008-5287-3766
M. Kodama orcid.org/0000-0002-6870-2450
A. Ikezawa orcid.org/0000-0002-8857-7159
H. Arai orcid.org/0000-0001-6695-637X

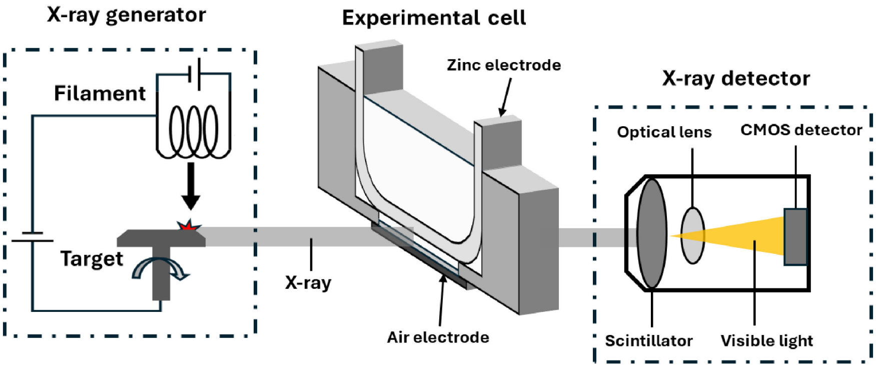

Figure 1. Schematic image of operando X-ray imaging system.

result in the performance degradation of zinc-air batteries and explore strategies to enhance their performance. For this purpose, a laboratory-scale X-ray microscope was used for two-dimensional transmission imaging of zinc-air batteries. Despite the lower output and resolution compared with a synchrotron X-ray techniques, the accessibility of the laboratory-scale X-ray microscope enabled us to explore a wide range of experimental conditions.

2. Experimental

2.1 Electrolyte preparation

To maximize ion conductivity, we used a 6 mol/L Potassium hydroxide (KOH) aqueous solution as the electrolyte.[12] KOH solid pellets (85 % purity, Tokyo Chemical Industry, Tokyo, Japan) were dissolved in pure water. For charge experiments, the electrolyte solution was previously saturated with ZnO to provide an ample supply of Zn ions in the electrolyte. ZnO powder (99 % purity, Hayashi Pure Chemical, Osaka, Japan) was added to KOH electrolyte and stirred for 170 hours. The saturated ZnO solution was then filtered using Polytetrafluoroethylene (PTFE) syringe filters to remove any residue, resulting in a zinc ion concentration of 0.58 mol/L in the electrolyte.[13] In each experiment, 250 µL of electrolyte was injected into the cell using a micropipette, as explained in the subsequent section.

2.2 Electrode preparation

The Zn electrodes consisted of a metal Zn plate (99.2 % purity, Nilaco, Tokyo, Japan) with a thickness of 0.3 mm. The surface of the zinc plates was polished with #800 Alumina sandpaper to remove the zincate layer. After polishing, the zinc plate was cut to a width of 2 mm, which is suitable for the X-ray observation cell.

The air electrodes consisted of a catalyst layer and a gas diffusion layer (GDL). The catalyst layer was a mixture of perovskite oxide powder ($La_{0.6}Ca_{0.4}CoO_3$, LCCO), carbon black powder (Vulcan XC 72) for electric conduction, and a PTFE dispersion (61 wt% in ethanol, Fluon AD911E) acting as a binder. The LCCO powder was synthesized via the sol-gel method,[14] with XRD conducted to verify existence of LCCO. The XRD pattern of LCCO closely matched that of a previous report.[14] The catalyst mixture was initially dispersed in a sufficient amount of ethanol and then dispersion dried on the surface of an aluminum disk at 60 °C, forming a uniform layer of the catalyst mixture. This catalyst layer has been confirmed to be chemically stable and functions as a catalyst for Oxygen Evolution Reaction (OER) and Oxygen Reduction Reaction (ORR) at potentials from −0.7 to +0.45 V vs. Hg/HgO, where the reactions of the air electrode in the zinc-air battery primarily occur.[14] A carbon paper GDL (0.28 mm thickness, Toray, Tokyo, Japan) was coated with the catalyst mixture by pressing the catalyst-attached aluminum disk at a temperature of 340 °C for 20 min. After coating, the thickness of the catalyst layer was 0.1 mm.

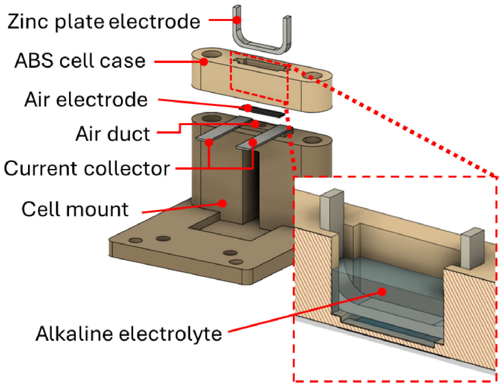

Figure 2. Schematic image of two-dimensional operando X-ray imaging cell.

2.3 Two-dimensional operando X-ray imaging system

A laboratory-scale X-ray microscope (Rigaku nano3DX) was employed for observing the experimental cell. Figure 1 is a schematic diagram of the X-ray observation system. X-rays in the microscope are generated by the inverse photoelectric effect. Electrons are emitted from a high-voltage filament and accelerated in a vacuum tube. Upon striking a rotating molybdenum target, a portion of the kinetic energy of the electrons is converted to X-rays. The acceleration voltage and tube current were 45 kV and 24 mA. The X-ray imaging area measured 1.6 × 1.2 mm, with a CMOS image sensor pixel size of 540 × 540 nm. The exposure time was 4 s for each image. To achieve sufficient X-ray transmission and high chemical resistance, the cells were fabricated with Acrylonitrile butadiene styrene (ABS) plastics. Figure 2 demonstrates the cell design. A three-dimensional (3-D) printer (Creator 3 pro, Flashforge) was used to produce the cell. The distance between the anode and cathode was 1 mm and the electrode area was 0.2 cm^2. Figure 3 shows an X-ray image of the cell, where the anode (black area at the top of the image) and cathode (double layer area at the bottom of the image) are clearly distinguished, along with the electrolyte. Notably, the upper area of the electrolyte is less bright than the lower area; the lower electrolyte area was designed to contain less electrolyte than the upper area to prevent electrolyte leakage. During the experiment, charge and discharge currents were applied using a potentio-galvanostat (Admiral Instruments, Squidstat Plus). Voltage and current shifts were recorded during X-ray observations. Before the experiment, the air electrode of the cell was aged by oxidation reaction of charging at 5 mA for 1 h. In the X-ray observation experiments, a new zinc electrode was used each time.

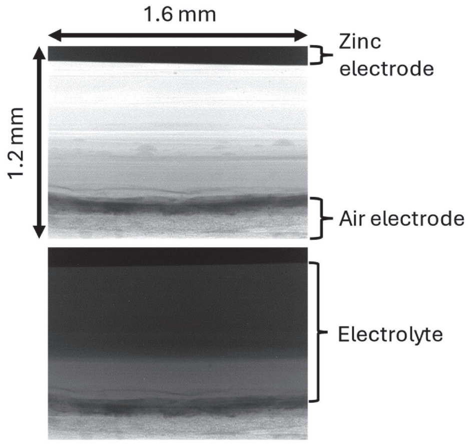

Figure 3. X-ray image without electrolyte (upper) and with electrolyte (lower).

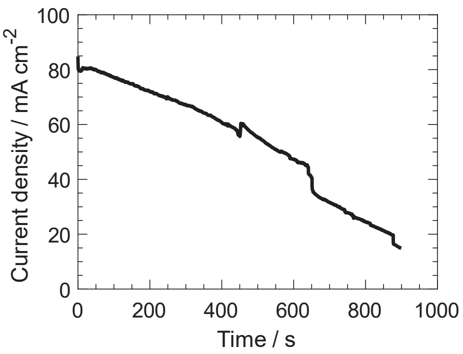

Figure 5. Time variation of current density at 0.8 V discharging.

3. Results and Discussion

In this study, we first describe the internal battery phenomena with operando X-ray imaging during the discharging process, during which the bubble formation occurs in the electrolyte. Subsequently, the internal battery phenomena are analyzed using operando X-ray imaging during the charging process, exploring various operating conditions. The aim is to elucidate zinc deposition behavior, specifically under conditions characterized by a high current density and low zinc ion concentration, which are known to induce dendrite growth.

3.1 Two-dimensional operando X-ray imaging of the discharging process

Operando X-ray imaging was performed on the cell under a constant voltage of 0.8 V during discharge. Figure 4 shows a series of X-ray images taken at different time intervals during the discharging process. From 0 to 540 s after the start of the discharge, round bright objects, which increased in size over time, were observed in the X-ray images. Bubbles were observed to form at both the zinc electrode and the air electrode. These objects are thought to be bubbles because of their reduced X-ray absorption. From 540 to 600 s after the start of the discharge, the bubbles formed at each electrode began to merge with each other, and the size of the bubbles increased. Finally, at 660 s, the region between the electrodes was brighter than the initial image at 0 s, indicating that the entire electrode space was filled with bubbles.

Figure 5 shows the time variation of the current density, measured concurrently with operando X-ray imaging. As with accumulation of bubble, the current density decreased monotonically in time. This voltage behavior indicates that bubbles covering the electrode surface suppress both electrochemical reactions on the surface of the electrode and the ohmic overpotential in the electrolyte surrounding the electrode.

The accumulation of bubbles between the electrodes is thought to occur for two reasons: 1. The ingress of external air from the air electrode, and 2. HER due to the corrosion of metallic zinc. While the ingress of external air from the air electrode is beyond the scope of this study, changes in the wettability of the air electrode due to electrochemical reactions during discharge are thought to be a possible cause. On the other hand, bubble generation due to side reactions at the air electrode can also be considered. The air electrode used in this study is known to have no significant side reactions within the range of −0.7 to +0.45 V vs. Hg/HgO.[14] Given that the theoretical voltage of the zinc air battery is 1.65 V and Fig. 5 shows results obtained at a constant voltage of 0.8 V, it can be seen that the overpotential of the entire cell is 0.85 V. Since the theoretical potential of the air electrode is 0.3 V vs. Hg/HgO, even if the entire overpotential of the cell occurs at the air electrode, the potential of the air electrode will not drop below −0.55 V vs. Hg/HgO. This means that the potential of the air electrode remains within the range where no side reactions occur.

In addition, although the exact mechanism of hydrogen evolution reaction (HER) at the zinc electrode is not fully understood, it is

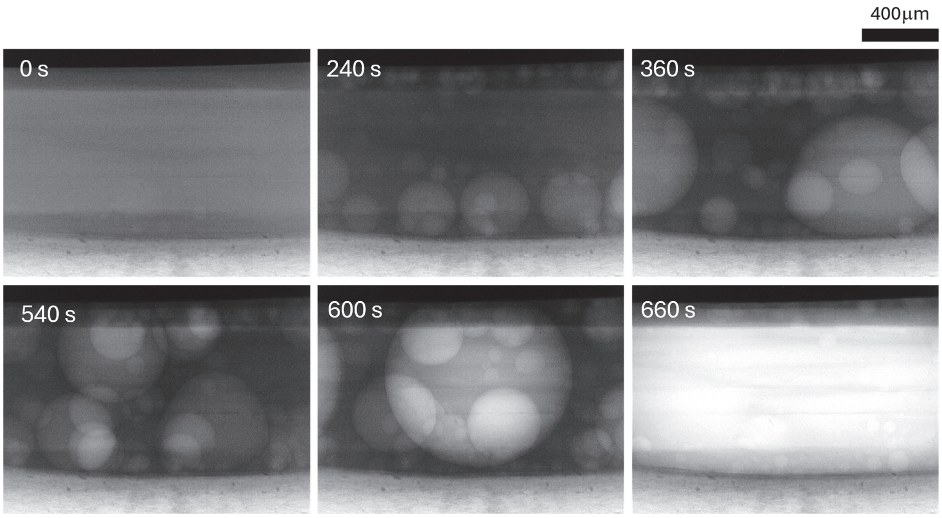

Figure 4. Time variation (0 to 660 s) of operando X-ray image at 0.8 V discharging.

considered that inhomogeneous reactions on the electrode surface cause some portions of metallic zinc to corrode in the electrolyte, leading to HER. Furthermore, as the electrode reactions proceed, newly exposed metallic zinc surfaces become corroded by the electrolyte, contributing to HER.

To investigate this phenomenon, we conducted discharge experiments by attaching a hydrogen gas concentration sensor (SGAS701, Renesas Electronics Corporation, Tokyo, Japan) to the cell. Figure 6a shows a schematic diagram of the cell with the hydrogen gas detection sensor attached. The hydrogen sensor is placed just above the electrolyte so that it can detect hydrogen gas released from the electrolyte as it diffuses toward the sensor, thus confirming the occurrence of hydrogen evolution. Figure 6b shows the change in hydrogen gas concentration over time in a cell discharging at 25 mA/cm^2. Before the discharge, from −200 to 0 s in Fig. 6b, the cell was in an OCV (Open Circuit Voltage) state, and the hydrogen gas concentration was 0 µmol/mol, indicating that no HER occurred. During the discharge, the hydrogen gas concentration increased with time, with a peak concentration of up to 64 µmol/mol observed. This peak is thought to be due to the sudden release of bubbles trapped in the electrolyte, causing a rapid increase in hydrogen concentration. This result confirms that hydrogen gas is contained in the bubbles generated between the electrodes.

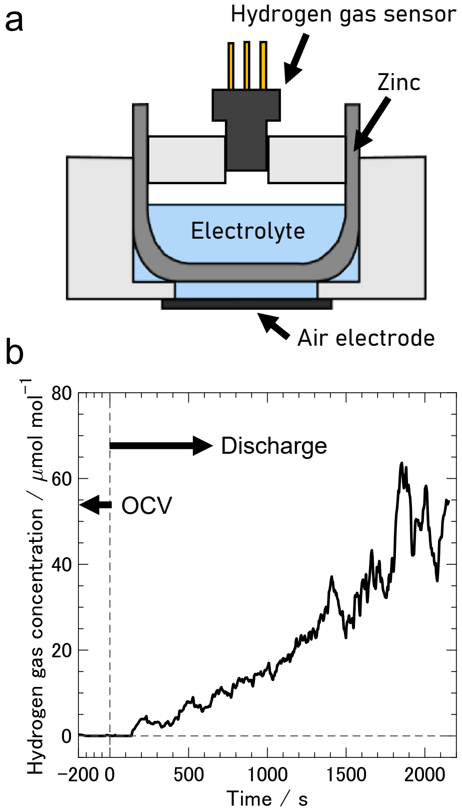

Figure 6. (a) Schematic diagram of hydrogen gas sensor in zinc air battery. (b) Time variation of hydrogen gas concentration at 25 mA/cm^2 discharging.

For the above reasons, the bubbles observed in the cell during the discharge process originate from hydrogen generated at the zinc electrode and air ingress from the air electrode. Although it is difficult to quantitatively evaluate the size and number of bubbles generated in the cell during discharge, and to determine the primary composition of these bubbles, it is clear that the bubbles generated during discharge tend to accumulate between the electrodes. The X-ray imaging results indicate that the bubbles generated between the electrodes do not escape and remain, which could adversely affect the discharge of the zinc-air battery. The X-ray images clearly show the behavior of the bubbles at each electrode, which will be useful for future studies aimed at elucidating the behavior of the bubbles.

3.2 Two-dimensional operando X-ray imaging of the charging process

X-ray imaging was conducted on zinc-air batteries under a constant current density. Figure 7 shows the X-ray images at a current density of 45 mA/cm^2. At 1860 s, a dark structure, thought to be highly dense zinc deposition, is seen on the zinc electrode surface. Between 1980 and 2760 s, the zinc deposition behavior changed, with significant growth toward the air electrode observed. The zinc structure resembles a tree-like structure, indicating zinc dendrite growth. Images captured after 2160 s show hydrogen bubble formation around the zinc dendrites. Figure 8 displays X-ray images at a higher current density of 100 mA/cm^2. At 660 s, dense zinc deposition is only observed near the zinc electrode. After 780 s, the zinc deposition behavior transitioned into dendritic form. Clear dendrite formation is observed in the image taken at 1200 s. Hydrogen bubble formation around zinc dendrites was also observed. These results demonstrate that dendrite deposition occurred earlier at a current density of 100 mA/cm^2 compared with 45 mA/cm^2. Figure 9 displays enlarged X-ray images of dendrite growth at the current density of 45 and 100 mA/cm^2. The tree-shaped structure of the dendrites is clearly shown in the X-ray images. No leakage or discoloration of the electrolyte was observed after charging.

Figure 10 shows the time variation of the cell voltage during constant current density charging at current densities of 50, 100, and 150 mA/cm^2. In the case of 50 mA/cm^2, the cell voltage gradually increases from 0 to 1500 s, after which a sharp increase is observed.

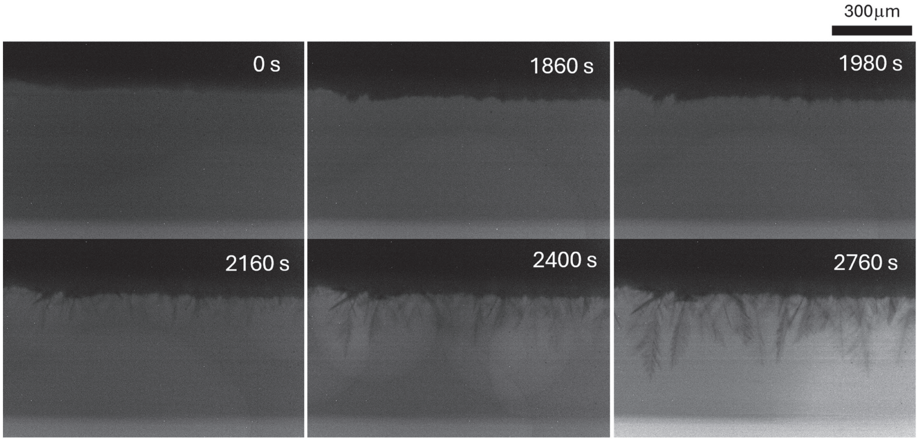

Figure 7. Time variation (0 to 2760 s) of operando X-ray image at 45 mA/cm^2 charging.

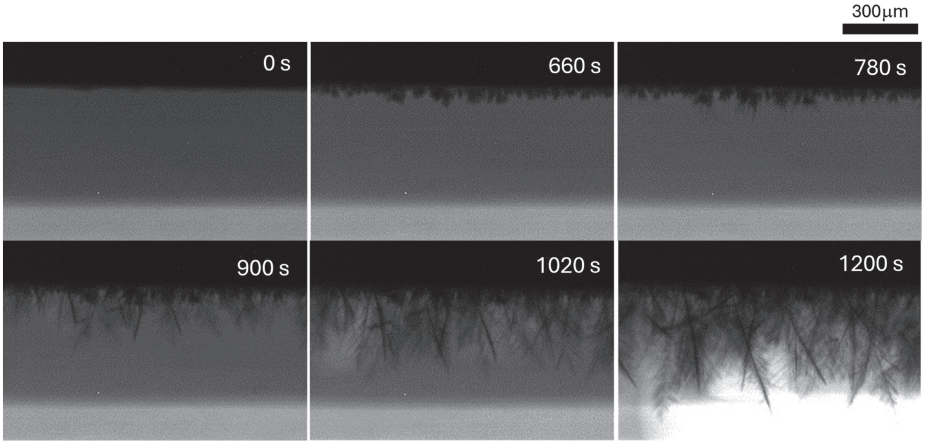

Figure 8. Time variation (0 to 1200 s) of operando X-ray image at 100 mA/cm^2 charging.

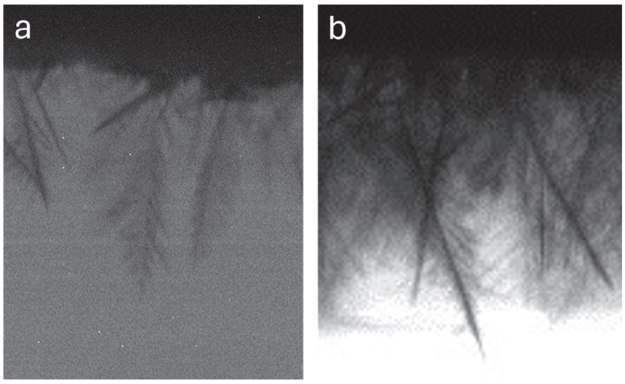

Figure 9. X-ray images of the dendrite at 45 mA/cm^2 charging and 100 mA/cm^2 charging.

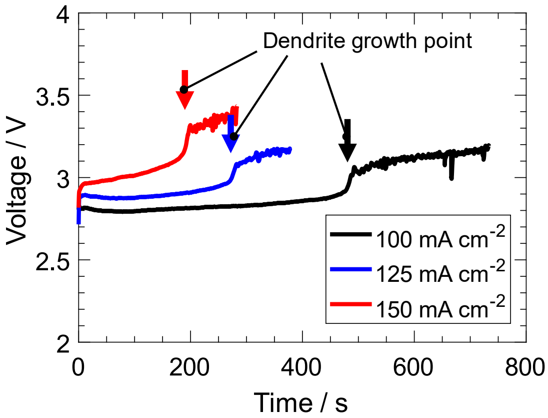

Figure 10. Time variation of cell voltage at 50, 100, and 150 mA/cm^2 charging.

Similar behavior is observed under current densities of 100 and 150 mA/cm^2, with the only difference being the time of the sharp increase. This sharp voltage increase is observed at 1500, 700, and 200 s for 50, 100, and 150 mA/cm^2, respectively. These instances correspond to the times when dendrite growth was observed in X-ray imaging. The voltage increase and high-frequency voltage instability are likely influenced by the change in zinc deposition behavior and subsequent dendrite shape. During dendrite growth, hydrogen bubble formation also occurs near the dendritic zinc. Because of the large surface area and sharp shape of the dendrites, the electrode reaction tends to be concentrated on dendritic zinc. Additionally, the generated bubbles are likely to be captured and accumulate in the complex structure of the dendrites. Consequently, even a small amount of hydrogen bubble generation near the dendrite can significantly reduce the electrode area, causing an overvoltage on the zinc electrode. This susceptibility of the electrode surface to hydrogen bubble behavior directly impacts cell voltage, resulting in high-frequency voltage instability.

Therefore, it can be said that zinc deposition during constant current charging occurs in two stages: initial dense zinc deposition on the electrode surface, followed by dendrite deposition in the later stages of charging. Dendrite deposition happens more quickly and with greater voltage instability as the charging current density increases.

Furthermore, hydrogen bubbles were observed during the charging, similar to those observed during the discharge. Since the cell used in this study is not well sealed, gas bubbles can easily escape, making it difficult to quantitatively compare the amount of hydrogen generated during the charge and discharge processes. This challenge will be the focus of future studies.

3.3 Two-dimensional operando X-ray imaging of the charging process under various working conditions

Results from charging at different current densities suggest that higher current densities tend to accelerate dendrite formation. In the charging process (Fig. 10), the initial zinc ion concentration was identical and the same amount of electrolyte was used for each cell, ensuring a constant total amount of zinc ions in the electrolyte. Under these conditions, a higher current density leads to a quicker depletion of zinc ions in the electrolyte, which means the zinc ion concentration decreases faster. Considering the early dendrite growth under a high current density (Fig. 10), it appears that changes in the zinc ion concentration are related to the growth time of dendrites.

To investigate this relationship further, operando X-ray imaging was conducted at a constant current with varying initial zinc ion concentrations in the electrolyte. Figure 11 shows the time variation of the cell voltage at a constant current of 30 mA/cm^2 with three different initial zinc ion concentrations. For an initial zinc ion concentration of 0.34 mol/L, the cell voltage remained almost constant from 0 to 1100 s. However, approximately 1200 s after charging started, there was a sudden increase in cell voltage. After 1200 s, the cell voltage exhibited high-frequency instability. Similar cell voltage behavior during charging was observed for other initial zinc ion concentrations of 0.44 and 0.53 mol/L, although the timing of the voltage increase was different, occurring at 2000 s and 2800 s, respectively. Figure 12 shows X-ray images around the transition

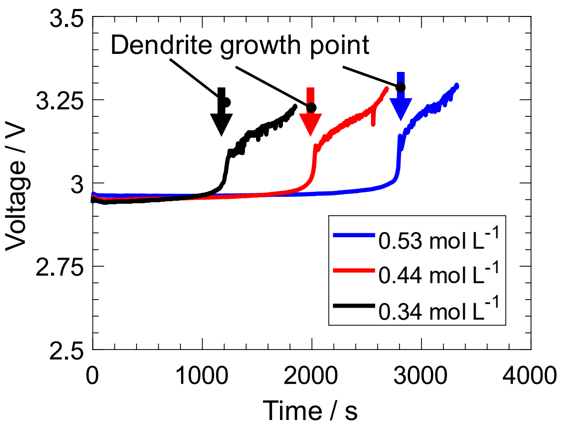

Figure 11. Time variation of cell voltage with initial zinc ion concentration of 0.34, 0.44, and 0.53 mol/L at 30 mA/cm^2 charging.

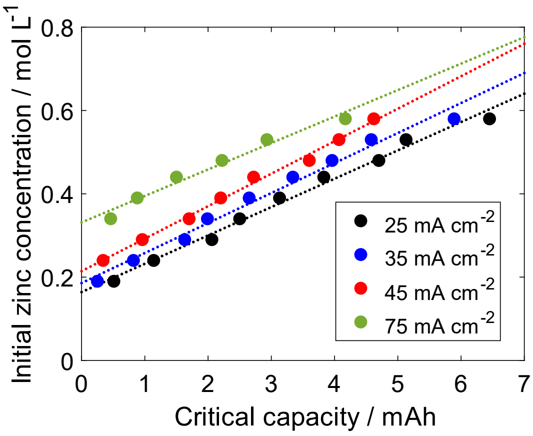

Figure 13. Relationship between the initial zinc ion concentration and critical capacity at various charging current densities.

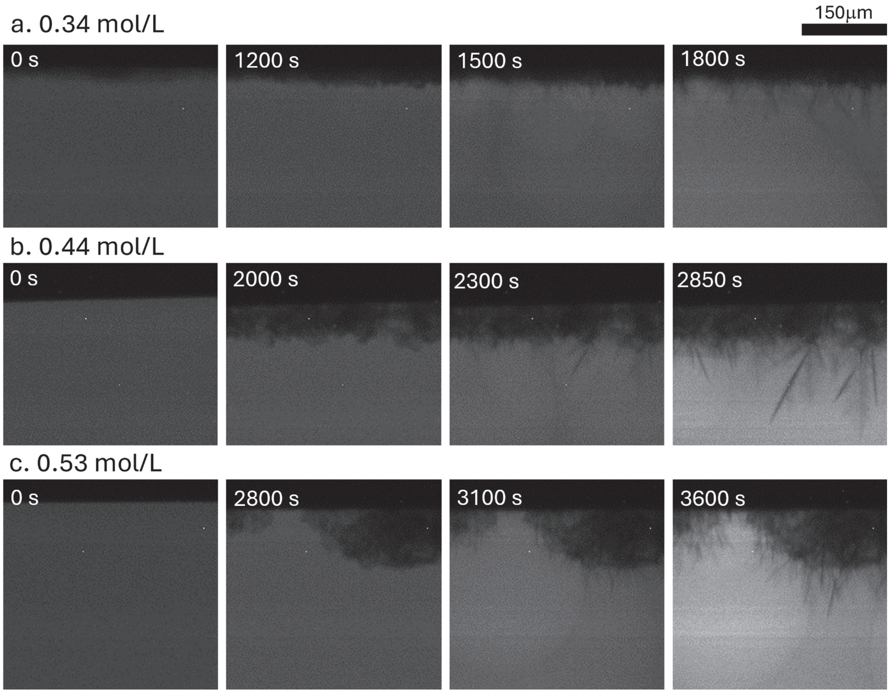

Figure 12. Time variation of operando X-ray image at the ion concentration of 0.34, 0.44, and 0.53 mol/L at 30 mA/cm^2 charging.

points of the zinc deposition behavior during charging experiments at various concentrations. In the experiment with an initial zinc ion concentration of 0.34 mol/L, the increase in charging voltage occurred around 1200 seconds, and no dendrites were observed in the X-ray image at this time. At 1500 s, sharp deposition began to appear on the zinc electrode, and by 1800 s, dendritic shapes were clearly distinguishable. Similar transitions in deposition behavior were observed at around 2000 s and 2800 s for the 0.44 and 0.53 mol/L conditions, respectively. The appearance of dendrites in the X-ray images did not perfectly coincide with the voltage increase, with a delay of about 300 s. This delay is because it takes time for dendrites to grow to a size detectable by X-ray imaging. Therefore, it is considered that the initiation of dendrite growth and the voltage increase practically occur at the same time. This result shows that charging in higher initial zinc ion concentrations requires longer times for dendrite growth, while lower initial zinc ion concentrations are expected to result in immediate dendrite formation upon charging.

Further concentration-based charging experiments were conducted across a wider range of concentrations and current densities. In the additional experiments, the initial zinc ion concentration of the electrolyte was set within the range of 0.15–0.58 mol/L and charging was conducted at current densities from 25 to 75 mA/cm^2. In these experiments, the dendrite growth point was identified using X-ray imaging, while the charging capacity at that point was defined as the critical capacity (mAh). Figure 13 shows the relationship between the initial zinc concentration and the critical capacity at various current densities. When charging at 25 mA/cm^2, the critical capacity shows a linear relationship with the initial zinc ion concentration. This linear relationship suggests that the conditions for dendrite formation are solely dependent on the zinc ion concentration at the time of charging, independent of the amount of zinc deposition and the duration of charging. Extrapolating this linear relationship to the y-axis for each current density allows for the determination of the zinc ion concentration at zero-critical capacity, indicating the point at which dendrites are likely to start

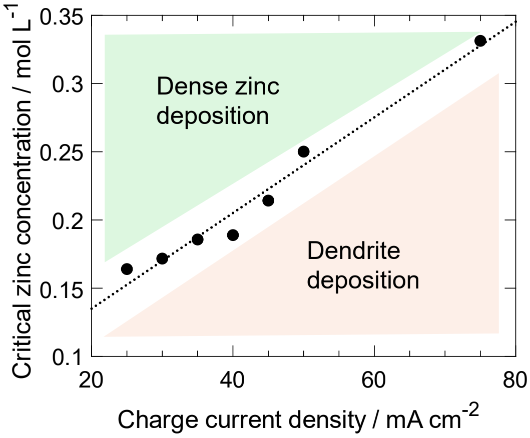

Figure 14. Critical zinc concentration as a function of charge current density.

forming immediately after charging starts. Defining this concentration as the critical concentration, the conditions for dendrite formation can be determined solely by the charging current density and critical concentration. Figure 14 shows the relationship between the critical zinc ion concentration and charging current density calculated from Fig. 13. Using this figure, the lowest zinc ion concentration at a specific current density at which dendrites do not form can be identified. The area above the dotted line (green region) in Fig. 14 represents battery operating conditions in which dendrites do not form. By controlling the zinc ion concentration and current density during charging, ensuring it remains in the green region, dendrite formation can be prevented, achieving stable charging of zinc-air batteries.

4. Conclusions

Through laboratory-scale two-dimensional operando X-ray imaging, we observed the internal behavior of zinc-air batteries under various operating conditions, i.e., current density and zinc ion concentrations, during both charging and discharging. Shape changes in both the electrodes and the electrolyte were observed in X-ray images, while the generation of bubbles between electrodes was observed during the discharge process. Along with bubble accumulation, the discharge voltage decreased monotonically over time. During the charging process, zinc deposition at the zinc electrode was observed. Based on X-ray images and changes in the charging voltage over time under constant current charging conditions, zinc deposition was confirmed to occur in two stages: initial dense deposition at the beginning of charging, succeeded by dendritic deposition in later stages. To explore the conditions required for dendritic deposition, charging experiments were conducted with varying initial zinc ion concentrations in the cell. It was confirmed that dendrites begin to form when the zinc ion concentration falls below a critical level, even with a fixed current density. The critical zinc ion concentrations for different charging current densities were experimentally measured, allowing us to determine the cell operational conditions required to prevent dendrite formation.

Acknowledgments

This work was supported by JSPS KAKENHI Grant Number 22H01412.

CRediT Authorship Contribution Statement

Wooseok Kang: Data curation (Lead), Investigation (Lead), Methodology (Lead), Writing – original draft (Lead)
Shumpei Kubota: Methodology (Equal)
Manabu Kodama: Methodology (Equal), Supervision (Equal), Writing – review & editing (Lead)
Atsunori Ikezawa: Methodology (Equal), Writing – review & editing (Equal)
Hajime Arai: Resources (Supporting), Writing – review & editing (Supporting)
Shuichiro Hirai: Funding acquisition (Lead), Project administration (Lead)

Conflict of Interest

The authors declare no conflict of interest in the manuscript.

Funding

Japan Society for the Promotion of Science: 22H01412

References

1. K. W. Leong, Y. Wang, M. Ni, W. Pan, S. Luo, and D. Y. C. Leung, *Renewable Sustainable Energy Rev.*, **154**, 111771 (2022).
2. A. G. Olabi, E. T. Sayed, T. Wilberforce, A. Jamal, A. H. Alami, K. Elsaid, S. M. A. Rahman, S. K. Shah, and M. A. Abdelkareem, *Energies*, **14**, 7373 (2021).
3. J. Zhang, Q. Zhou, Y. Tang, L. Zhang, and Y. Li, *Chem. Sci.*, **10**, 8924 (2019).
4. Y. Zuo, K. Wang, P. Pei, M. Wei, X. Liu, Y. Xiao, and P. Zhang, *Mater. Today Energy*, **20**, 100692 (2021).
5. J.-C. Riede, T. Turek, and U. Kunz, *Electrochim. Acta*, **269**, 217 (2018).
6. C. Yang, X. Liu, K. Yang, Y. Lai, K. Zhang, and Z. Tian, *J. Solid State Electrochem.*, **25**, 611 (2021).
7. Z. Xu and M. Wu, *Batteries*, **8**, 117 (2022).
8. A. Ikezawa, M. Horiuchi, and H. Arai, *J. Power Sources*, **507**, 230291 (2021).
9. R. Franke-Lang, T. Arlt, I. Manke, and J. Kowal, *J. Power Sources*, **370**, 45 (2017).
10. D. Deckenbach and J. J. Schneider, *J. Power Sources*, **488**, 229393 (2021).
11. V. Yufit, F. Tariq, D. S. Eastwood, M. Biton, B. Wu, P. D. Lee, and N. P. Brandon, *Joule*, **3**, 485 (2019).
12. R. Gilliam, J. Graydon, D. Kirk, and S. Thorpe, *Int. J. Hydrogen Energy*, **32**, 359 (2007).
13. A. L. Zhu, D. P. Wilkinson, X. Zhang, Y. Xing, A. G. Rozhin, and S. A. Kulinich, *J. Energy Storage*, **8**, 35 (2016).
14. X. Li, W. Qu, J. Zhang, and H. Wang, *J. Electrochem. Soc.*, **158**, A597 (2011).